1   Stratigraphy and Isotope Geochemistry of the pre-Sturtian Ugab Subgroup, Otavi Group, northwestern

2   Namibia

3   Kelsey G. Lamothe[1], Paul F. Hoffman[2,3], J. Wilder Greenman[1], and Galen P. Halverson[1]

4   *1: Department of Earth & Planetary Sciences, McGill University, QC H3A 0E8, Canada*

5   *2: School of Earth & Ocean Sciences, University of Victoria, Victoria, BC V8P 5C2, Canada*

6   *3: Department of Earth & Planetary Sciences, Harvard University, Cambridge, MA 01238, USA*

7   **Abstract**

8   The Islay carbon isotope anomaly is a late Tonian negative $\delta^{13}C$ excursion that has been documented in

9   marine carbonates globally. It has in the past been thought to be causally linked to the onset of

10   Cryogenian glaciation ca. 717 Ma. However, recent work suggests that this anomaly is instead closer to

11   ca. 739–735 Ma and that it may be one of two distinct late Tonian isotope anomalies. Here we present the

12   litho- and chemo-stratigraphy of the late Tonian Ugab Subgroup of the Otavi Group in northwestern

13   Namibia. Carbon isotope data from two separate outcrop belts, the Summas Mountains and the Vrede

14   Domes, indicate that the Ugab Subgroup strata exposed in the former inlier are older than those of the

15   latter, with only approximately 100 metres of stratigraphic overlap. We use detailed measured sections to

16   develop a sequence stratigraphic framework for the Ugab Subgroup in each outcrop belt, and correlate

17   strata across the two exposures to construct a composite carbonate $\delta^{13}C$ record for the late Tonian in

18   Namibia. This carbon isotope profile of the Ugab Subgroup shows two separate pre-Sturtian negative

19   anomalies, consistent with findings in northern Canada, Svalbard, Scotland, and Ethiopia. Our results are

20   an important contribution to the pre-Cryogenian carbon isotope record, as these data may serve as the first

21   definitive documentation of both anomalies within a single basin.

22   Keywords: Neoproterozoic; carbon isotopes; carbonates; stratigraphy

23

24

Introduction

The Neoproterozoic Era (1000-541 Ma) was a time of enormous climatic fluctuations that included at least two global glaciations, often termed 'Snowball Earth' events, each followed by extreme greenhouse conditions (Kirschvink 1992; Hoffman et al., 1998). The Neoproterozoic also records at least six globally correlative significant negative excursions in the marine carbonate carbon isotope record ($\delta^{13}C_{carb}$), which are superimposed on a long-term baseline carbon isotope enrichment of ~5‰ that persisted until the Cambrian Period (~541 Ma) (Halverson et al., 2005; Halverson et al., 2018a). Much of this time is characterized by significant tectonic reorganization, with the lengthy breakup of the equatorially-centered supercontinent Rodinia (ca. 830-720 Ma) and following assembly of Gondwana (Hoffman, 1991, 1999; Meert and Lieberman, 2008; Pisarevsky et al., 2003). Additionally, the Neoproterozoic features important advances in biological evolution, including expansion in eukaryotic diversity observed in the fossil record beginning ca. 800 Ma (Porter, 2004) and the appearance of the first macroscopic metazoans ca. 571 Ma (Pu et al., 2016).

Although the Neoproterozoic geological record has been dramatically refined by new stratigraphic and geochronological studies in the past two decades, the study of the Precambrian sedimentary record remains a challenge due to the limited biostratigraphic record and relative scarcity of well-preserved successions. Consequently, division of the Precambrian into meaningful and accurate units of geologic time poses an ongoing challenge. Following establishment of the basal Ediacaran Global Stratotype Section and Point (GSSP) at the base of cap carbonates overlying Marinoan (ca. 635.5 Ma) glacial deposits (Knoll et al., 2004), an international effort is now underway to replace the 720 Ma Tonian-Cryogenian Global Standard Stratigraphic Age (GSSA) with a GSSP. However, this effort is complicated by the typically erosional nature of the lower Cryogenian boundary (Shields-Zhou et al., 2016; Shields et al., 2018). It is mandated that the Cryogenian GSSP should be beneath the oldest glaciogenic deposits and it is broadly agreed that its placement will be guided by high resolution chemostratigraphic data,

49   specifically the carbon isotope record (Shields-Zhou et al, 2016). Therefore, improved records of pre-

50   Sturtian strata worldwide are required in order to select the most appropriate location for the GSSP.

51   A potentially important chemostratigraphic marker for selecting this GSSP is the pre-Sturtian Islay

52   anomaly, a negative carbon isotope excursion has been observed in late Tonian carbonate successions in

53   multiple locations on many paleocontinents. The purported Islay anomaly marks a drop in $\delta^{13}C_{carb}$ of

54   approximately 10‰; in some locations, it corresponds also to a small coeval decline in $\delta^{13}C_{org}$ (Hoffman

55   et al., 2012; Strauss et al., 2014). The Islay anomaly has been considered to be analogous to the better-

56   documented pre-Marinoan Trezona anomaly (McKirdy et al., 2001; Halverson et al., 2002), and by

57   extension, inferred to record a perturbation to the carbon cycle that is genetically linked to the onset of the

58   first (Sturtian) Neoproterozoic Snowball Earth event (e.g., Halverson and Shields, 2011). However,

59   debate as to the cause, synchronicity, and even primary nature of these pre-glacial anomalies persists.

60   Furthermore, new age constraints for the Islay anomaly have called into question the assumption of a

61   causal linkage between the mechanism that generated the Islay anomaly and initiated the Cryogenian

62   glaciation. A late Tonian carbon isotope anomaly in northern Ethiopia thought to be correlative to the

63   global Islay anomaly is now precisely constrained by a U-Pb age of 735.25 ± 0.88 Ma from a volcanic

64   layer just metres above the nadir of the anomaly (MacLennan et al., 2018). This age agrees with Re-Os

65   ages of 739.9 ± 6.1 Ma and 732.2 ± 3.9 Ma bracketing an anomaly of similar magnitude in northwestern

66   Canada (Rooney et al., 2014; Strauss et al., 2015), and followed by a complete recovery to baseline $\delta^{13}C$

67   values before the onset of the Sturtian glaciation ca. 717 Ma. However, recent work in Scotland on a

68   conformable transition from pre-glacial carbonates into glacial diamictite shows a negative carbon isotope

69   excursion of similar magnitude in strata that are interpreted to be continuous and conformable with early

70   Cryogenian glacial deposits, suggesting an age much closer to 717 Ma (Fairchild et al., 2018; Ali et al.,

71   2018). These ages and observations have raised speculation of the existence of two separate 'Islay

72   anomalies', and highlights the need for more detailed end-Tonian $\delta^{13}C$ records (Halverson et al., 2018a).

73   Despite the many documented occurrences globally of pre-Sturtian $\delta^{13}C$ excursions, the 'Islay' anomaly

74   has not been conclusively reported in the Otavi Group of northwestern Namibia, a succession which

75   played a key role in the development of the Snowball Earth Hypothesis (e.g. Hoffman et al., 1998). The

76   Ugab Subgroup of the Otavi Group comprises the most immediately pre-Cryogenian strata of

77   northwestern Namibia and is only present on the distal foreslope of and in the basin adjacent to the Otavi

78   Platform. Negative $\delta^{13}C_{carb}$ values have been documented in the Ugab Subgroup where it outcrops in the

79   Summas Mountains region (Hoffman and Halverson, 2008; Hoffman, unpublished data), but their affinity

80   with the Islay anomaly is uncertain, and the stratigraphic relationships between the Ugab Subgroup strata

81   in the Summas Mountains and other exposures of the subgroup are not well-defined. Here we will present

82   a depositional framework and regional correlations for the pre-Cryogenian Ugab Subgroup and use these

83   to integrate the existing carbon isotope data with our new results to present an updated carbon isotope

84   profile for the Ugab Subgroup, which is consistent with the recent proposal of the existence of two

85   discrete pre-Sturtian negative $\delta^{13}C$ anomalies.

86   **Geologic Context**

87   Early during the fragmentation of Rodinia, north-south crustal stretching opened a rift basin between the

88   Congo craton and its conjugate margin to the south. Initial rifting, ca. 900-760 Ma, resulted in the

89   deposition of the Nosib Group as siliciclastic sediments were shed southward off the Congo craton into

90   the emerging rift basin (Miller, 2008). As extension continued episodically for ~140 Ma, a

91   paleotopographic high called the Makalani Ridge developed in the basin from uplift and back-rotation

92   along a large-scale normal fault. This faulting divided the Makalani sub-basin to the north from the Outjo

93   sub-basin to the south. Intensity of the crustal stretching increased southwards (Henry et al., 1990),

94   causing differentiation between the Makalani sub-basin, into which the Ombombo Subgroup was

95   deposited, and the deeper Outjo sub-basin, in which bimodal volcanism was followed by deposition of

96   intercalated siliciclastic sediments and peritidal carbonates of the Ugab Subgroup. During the Sturtian

97   glaciation, a second paleotopographic high, the Huab Ridge, formed south of the Makalani Ridge. Crustal

98   stretching ceased during the interglacial interval ca. 650 Ma, and thermal subsidence took over as the

99   dominant control on the basin (Halverson et al., 2002), resulting in the development of a stable, shallow-

100   water carbonate platform with a shelf-break at the scarp of the Huab ridge. A foreslope south of the shelf

101   break transitioned into the deep-water Outjo sub-basin, and the Hoanib Lagoon was established to the

102   north. Ensuing thermal subsidence on the passive margin accommodated nearly two kilometres of almost

103   entirely carbonate strata on the Otavi platform. A comprehensive review of the Otavi Group stratigraphy

104   in northwestern Namibia is provided by Hoffman and Halverson (2008).

105
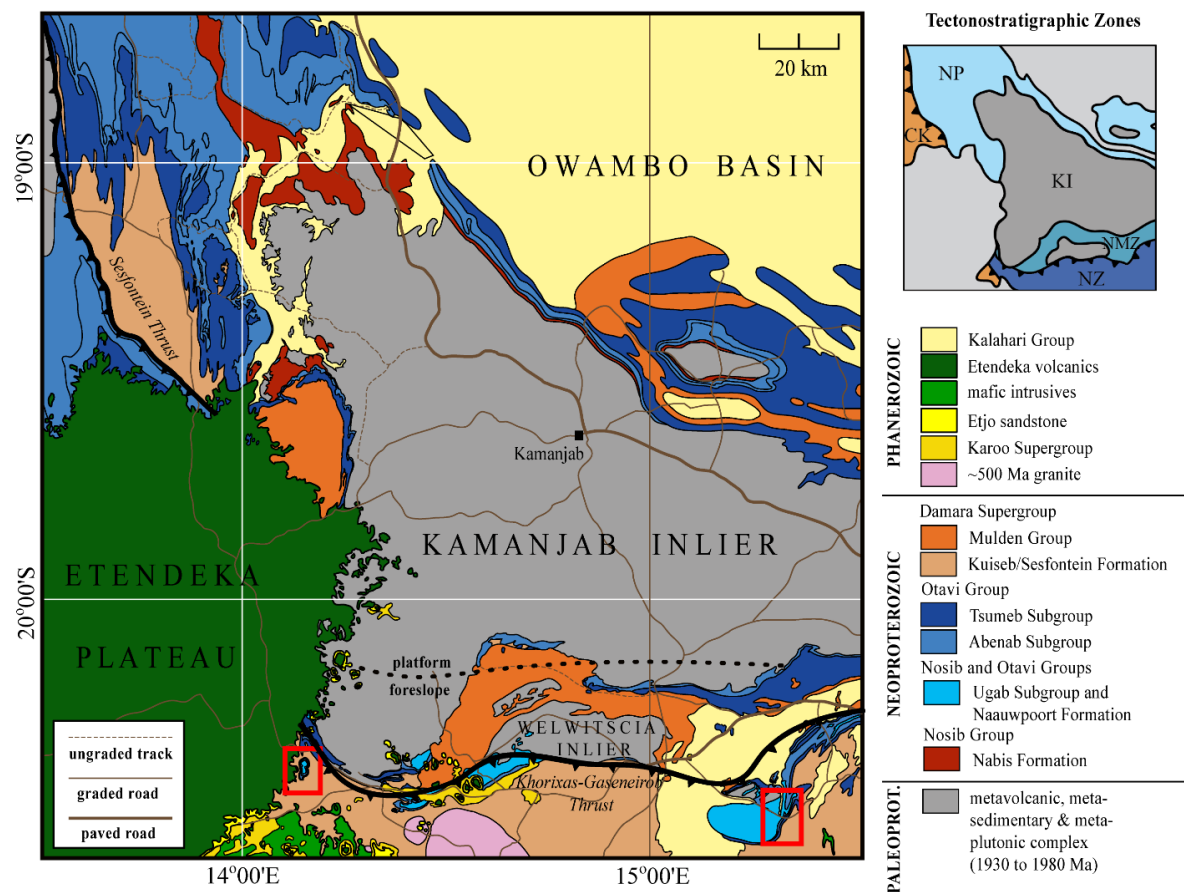
106   *Figure 1: Geological map of the southern Kunene region area around the Kamanjab inlier, from*

107   *Hoffman and Halverson (2008). Field areas outlined in red boxes; Vrede Domes to the left and the*

108   *Summas Mountains to the right. Small map in top right corner shows the tectonostratigraphic zones of*

109   *this same area, where NP= Northern Platform, NMZ= Northern Margin Zone, NZ= Northern Zone, KI=*

110   *Kamanjab Inlier, and CK= Central Kaoko Zone.*

111   Miller (1983, 2008) divided Namibia into tectonostratigraphic zones associated with the Damara Orogen,

112   (see *Figure 1*), with alternate names for the zones offered by Hoffmann et al. (1989). The Otavi Group

113   lies within three of these tectonostratigraphic zones: the Northern Platform, the Northern Margin Zone,

114   and the northernmost Northern Zone, where there is a gradational transition into the basinal correlatives

115   of the Swakop Group (Miller, 2008).

116   The Northern Platform or Otavi Platform contains the platform facies rocks of the Otavi Group. Damara

117   Supergroup successions are exposed along the western and southern rim of the Northern Platform and

118   extend beneath Phanerozoic cover in the Owambo Basin to the east. The western border of the Northern

119   Platform is defined by the east-vergent Sesfontein Thrust, which juxtaposes metamorphosed Otavi Group

120   from the internal zone of the Kaoko Belt against the less deformed fold and thrust belt. The southern

121   border is the platform-to-slope transition; it is well-exposed along the southern flank of the Kamajab

122   Inlier. The Northern Margin Zone is a thin strip of foreslope deposits rimming the southern edge of the

123   Northern Platform. The Northern Margin Zone is separated from the Northern Zone to the south by the

124   Khorixas-Gaseneirob Thrust. The Northern Zone or Outjo Zone made up part of the seafloor of the Outjo

125   basin during rifting and spreading. When the Kalahari and Congo cratons collided ca. 550 Ma, the

126   Northern Zone was thrust northward along the Khorixas-Gaseneirob Thrust onto the Northern Margin

127   Zone. It is within the Northern Zone that the Ugab Subgroup outcrops.

128   In the northernmost Northern Zone, the Ugab Subgroup forms the base of the Otavi Group and sits

129   stratigraphically between the volcanic Naauwpoort Formation and the glaciogenic Chuos Formation. The

130   Ugab Subgroup consists mainly of peritidal carbonates intercalated with siliciclastics. Its relationship to

131   the Ombombo Subgroup of the Otavi Platform is still not fully understood, but a U-Pb zircon age of 746

132   ±2 Ma from an ash-flow tuff in the Naauwpoort Formation (Hoffman et al., 1996) suggests that the Ugab

133   Subgroup must be at least 15 m.y. younger than the upper Devede Formation, which contains a tuff dated

134   (U-Pb zircon) at 760±1 Ma (Halverson et al., 2005). The youngest possible age for the top of the Ugab

135   Subgroup can be inferred from a maximum age constraint of 717.4±0.2 Ma for the onset of the Sturtian

136   glaciation (Macdonald et al., 2010, 2018; MacLennan et al., 2018).

137   Miller (1980; 2008) divided the Ugab Subgroup of the NZ into the Okotjize and Orusewa Formations,

138   with the former being a carbonate-dominated and the latter being siliciclastic-dominated. The Okotjize

139   Formation is described as a succession of dolostone interbedded with schist and marly schist that is

140   locally hundreds of metres thick but laterally pinches out. The Okotjize Formation is conformably

141   overlain by the Orusewa Formation, which generally consists of schist overlain by a quartzite that is

142   highly variable in degree of sorting and composition that has been suggested to represent deposition of

143   eroded material associated with the pre-Sturtian fall in sea-level (Miller, 2008).

144   **Methods**

145   *Field Work*

146   Field work was executed in the two outcrop belts with the best exposures of the Ugab Subgroup: the

147   Summas Mountains and the Vrede Domes. In each field area, many closely-spaced sections were

148   measured to work out stratigraphic relationships, and carbonate samples were collected from several

149   sections and partial sections were sampled opportunistically (sampling interval of 3–4 m) for carbon

150   isotope analysis.

151   We synthesized these new stratigraphic logs and data with previously published (Hoffman and Halverson,

152   2008) and unpublished results of many past field seasons of work done in the Vrede Domes and Summas

153   Mountains regions, including detailed measured sections and $\delta^{13}C_{carb}$ profiles.

154   *Carbon and oxygen isotope analysis*

155   Carbonate samples were cut using a diamond lapidary blade to expose unweathered surfaces, then rinsed

156   and dried. A table drill was used to collect small amounts of fine powder, along lamination where visible,

157   from cut surfaces of the samples for $\delta^{13}C_{carb}$ and $\delta^{18}O_{carb}$ analyses. Veins and fractures were avoided.

158   Approximately 120 µg of powder from each sample was weighed out for analysis on a Nu Instruments

Perspective mass spectrometer coupled to a NuCarb automated carbonate preparation device, at McGill University. Carbon and oxygen isotope ratios were measured simultaneously in dual inlet mode. Batches contained 40 samples with 10 in-house geostandards regularly interspersed. The samples were heated to 70°C and sequentially reacted with phosphoric acid (H_3PO_4) to produce CO_2, which was then cryogenically isolated. Isotopic ratios of the CO_2 were measured against reference gas, and $\delta^{13}C_{carb}$ and $\delta^{18}O_{carb}$ were calculated and calibrated to VPDB, with a 1σ precision of <0.05‰.

The Summas Mountains Inlier

The Summas Mountains Inlier (*Figure 2*) is located in the Northern Zone approximately 30 km ESE of the town of Khorixas. It is a former volcanic center and one of the two sources of the Naauwpoort Formation rift-related volcanics (Miller, 1980). The Naauwpoort Formation in the Summas Mountains consists mainly of peralkaline to alkaline rhyolitic tuffs, with minor mafic volcanics (Miller, 1980). A U-Pb zircon date of 746±2 Ma exists for an ash-flow tuff collected approximately 1000 metres stratigraphically below the contact with the Ugab Subgroup (Hoffman et al., 1996). At the core of the
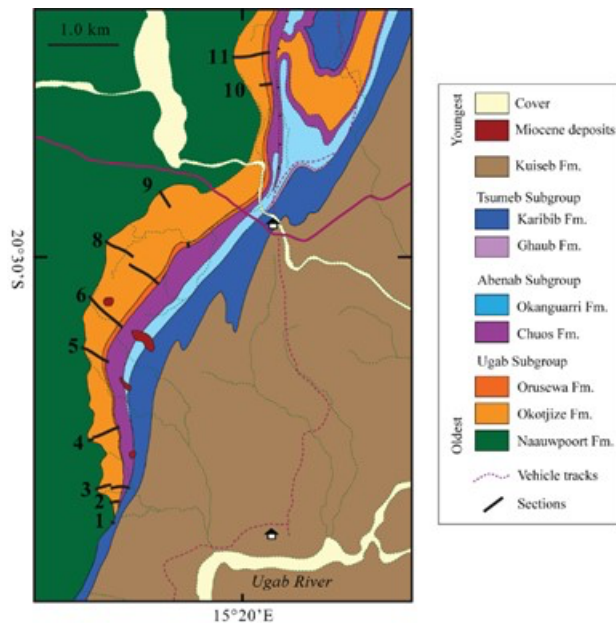
Figure 2: Geological map of the Summas Mountains with measured section locations marked (see Figure 3 for corresponding sections). Modified from Hoffman et al. (2018).

175 inlier, proposed to be a cauldron-subsidence structure (Guj, 1974), the cumulative thickness of the

176 rhyolitic ash-flow tuffs exceeds 6km and the base is not visible (Miller, 1974; 1980). The Ugab Subgroup

177 outcrops on the eastern edge of the Summas Mountains, where it paraconformably overlies Naauwpoort

178 Formation volcanic rocks and lies beneath the Chuos Formation, separated by a low-angle unconformity.

179 The Chuos Formation here is continuous and ranges in thickness from at least 25 metres to over 300

180 metres.

181 ***Ugab Subgroup Lithostratigraphy in the Summas Mountains***

182 A composite section (P2538) of the Ugab Subgroup in the Summas Mountains was previously generated

183 from overlapping sections just south of the Huab River on Loewenfontein Farm (***Figure 3***; Hoffman and

184
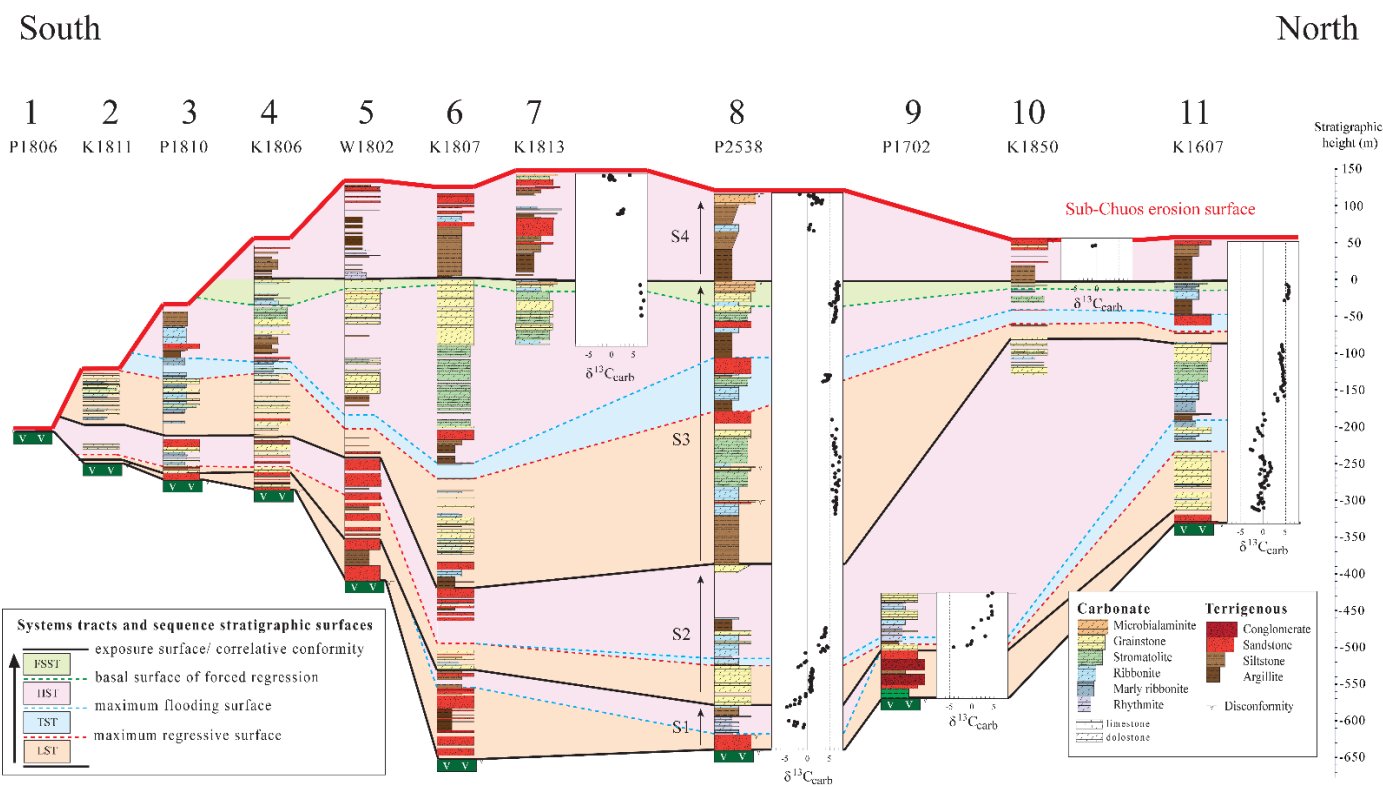
185 *Figure 3: Stratigraphic sections of the Ugab Subgroup in the Summas Mountains, with base of Okotjize*

186 *Formation used as datum. Section locations marked on Figure 2. S1-4 indicate the identified depositional*

187 *sequences, as described in text.*

188   Halverson, 2008). This section comprises 20 shallowing-upward depositional cycles separated by

189   flooding surfaces or, less commonly, by subaerial exposure surfaces.

190   Six additional full sections of the Ugab Subgroup and three partial sections were measured for this study.

191   The southernmost sections (K1806, P1810, and K1811) show erosional truncation beneath the Chuos

192   Formation increasing to the south, and complete erosion of the Ugab Subgroup in section P1806 (*Figure*

193   *3*).

194   A coarse siliciclastic unit, consisting dominantly of quartz arenite, is found at the base of all sections with

195   the exception of K1811, where the base is not exposed. This basal unit is highly variable both in thickness

196   and number of parasequences recorded. Directly overlying the coarse siliciclastic unit in P2538 are four

197   small-scale (<10 metres thick) deep-water carbonate parasequences that are absent in the other sections

198   but may coincide with a gap in exposure. Alternatively, the fine carbonate unit could have been squeezed

199   out during deformation, as it is rheologically weaker than the bracketing units of sandstone. The next

200   several hundred metres of section are dominated by carbonate cycles, commonly interbedded with

201   argillite or siltstone in the northern sections. Sandstone-capped cycles in the south progressively become

202   more carbonate-rich up-section. Near the top of the sections, a major flooding surface marks a transition

203   to dominantly fine-grained siliciclastics at the base of the Okotjize Formation.

204   *Sequence Stratigraphic Architecture of the Summas Mountains*

205   Four third-order depositional sequences (Krapez, 1996), denoted as S1-S4, were identified and are shown

206   in *Figure 3*. We interpret the basal coarse siliciclastic unit as a lowstand systems tract (LST), overlain in

207   P2538 by a thin highstand systems tract represented by several fine carbonate parasequences. The end of

208   this deep-water unit marks the transition to sequence 2, which begins with a unit of variable thickness

209   consisting dominantly of grainstone to the north and sandstone to the south that comprise the LST. A

210   maximum flooding surface (MFS) above a thick carbonate unit marks the base of a thick HST, consisting

211   of at least five parasequences of ribbonite or marly ribbonite, or less commonly argillite, grading into

212   grainstone to the north and sandstone to the south. The base of a thick siltstone unit in P2538 is

213   interpreted as an exposure surface, overlain by an LST at the base of sequence 3. The top of the LST is a

214   flooding surface above a sandstone unit. This flooding surface marks the beginning of a TST consisting of

215   two parasequences. The MFS is within the thick argillite unit that overlies sandstone. The HST consists

216   dominantly of fine-grained siliciclastic sediments at the base and carbonates at the top. It is overlain by an

217   FSST that culminates in grainstone and microbialaminites with an exposure surface, which marks the

218   base of sequence 4 and a major flooding surface.

Carbon Isotope Results from the Summas Mountains

220   Carbonate samples were collected from one full section and three partial sections in the Summas

221   Mountains and integrated with existing data from P2538. Cross-plots of carbon and oxygen isotope data

222   from all sections from the Summas Mountains show some degree of correlation, implying the potential

223   for moderate to high levels of diagenetic overprinting (***Figure 4***). Alteration by meteoric water has been

224   documented to drive both oxygen isotope ratios and carbon isotope ratios (to a lesser extent) to more

225   negative values (Allan and Matthews, 1982). However, the carbon isotope data from the full section
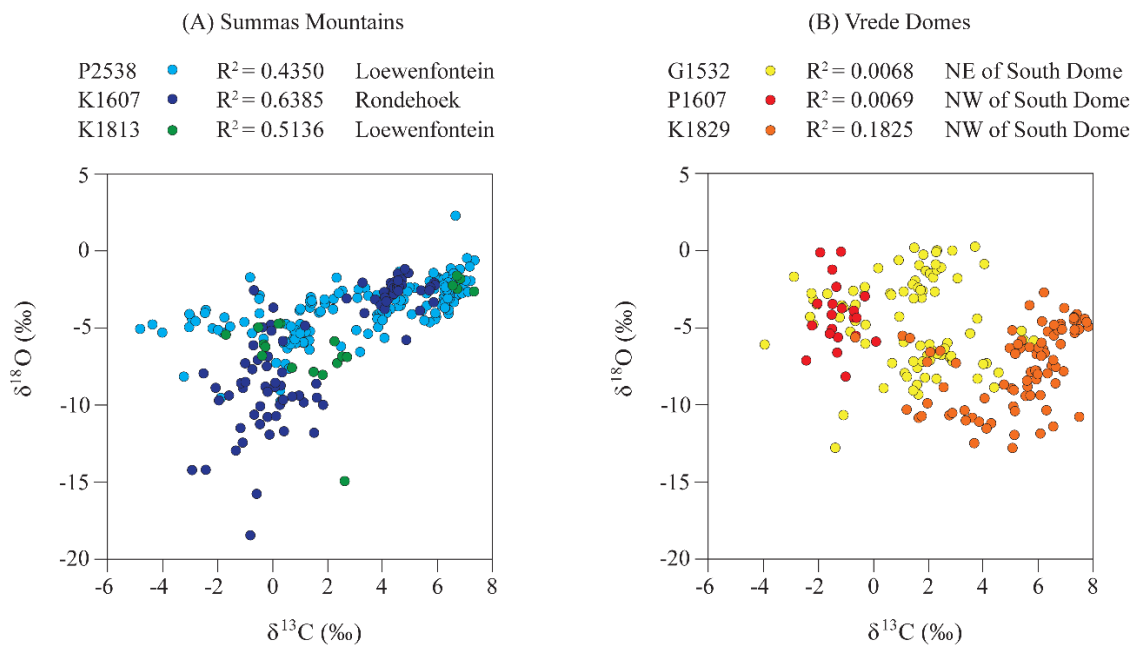
227   *Figure 4: Carbon and oxygen isotope cross-plots of Ugab Subgroup sections from the Summas*

228   *Mountains (A) and the Vrede Domes (B).*

229 at Rondehoek Farm from this study (K1607) closely matches the composite section (P2538) measured

230 previously on Loewenfontein Farm approximately five kilometres to the south (Hoffman and Halverson,

231 2008) (*Figure 3*). Both sections show a double-nadir negative anomaly and a recovery to ~5‰ in the

232 basal 150 metres of section, followed by $\delta^{13}C$ remaining relatively stable around 5‰ for several hundreds

233 of metres.

234 The nadir of the first peak of the basal anomaly reaches nearly -5‰ in Loewenfontein section P2538.

235 The full anomaly is not recorded in Rondehoek section K1607, and the ascending arm begins from -3‰.

236 In both sections, $\delta^{13}C$ rises to approximately 1 ‰ before abruptly dropping back to -3 ‰ directly above a

237 flooding surface. Partial section P1702 also captures a portion of this apparent double-peaked negative

238 anomaly. Section K1607 records a drop in $\delta^{18}O$ coinciding with the basal anomaly, as well as a large

239 increase in the scatter of $\delta^{18}O$ that is not observed in $\delta^{13}C$.

240 Carbon isotope values then rise to a plateau around 5‰, at which they remain for nearly 500 metres.

241 Carbonates from the top of the Loewenfontein section, absent in the Rondehoek section, record $\delta^{13}C$

242 descending back towards 0‰, and drop to negative values within a few metres of the subglacial erosion

243 surface. This descent coincides with a considerable decrease in $\delta^{18}O$, signifying that alteration is likely

244 and the negative trend in $\delta^{13}C$ should be treated cautiously. A partial section, K1850, measured just half a

245 kilometre south of the full Rondehoek section, contains a thin carbonate grainstone unit within the

246 uppermost sandstone unit, with $\delta^{13}C$ values just below 0‰.

247 **The Vrede Domes**

248 The Vrede Domes (*Figure 5*) are a pair of doubly plunging anticlines located in the Northern Zone,

249 approximately 80 km west of the town of Khorixas (*Figure 1*). They are interpreted to have formed from

250 interference folding during three phases of deformation, beginning with N-S shortening followed by E-W

251 shortening associated with the Kaoko orogen, and finally ENE-WSW shortening associated with the

252 Damara orogen (Maloof, 2000). The domes expose Otavi Group strata, with the Ugab Subgroup in the

253 core. The Ugab Subgroup here shows a rapid lateral transition from coarse siliciclastic deposition in the

254
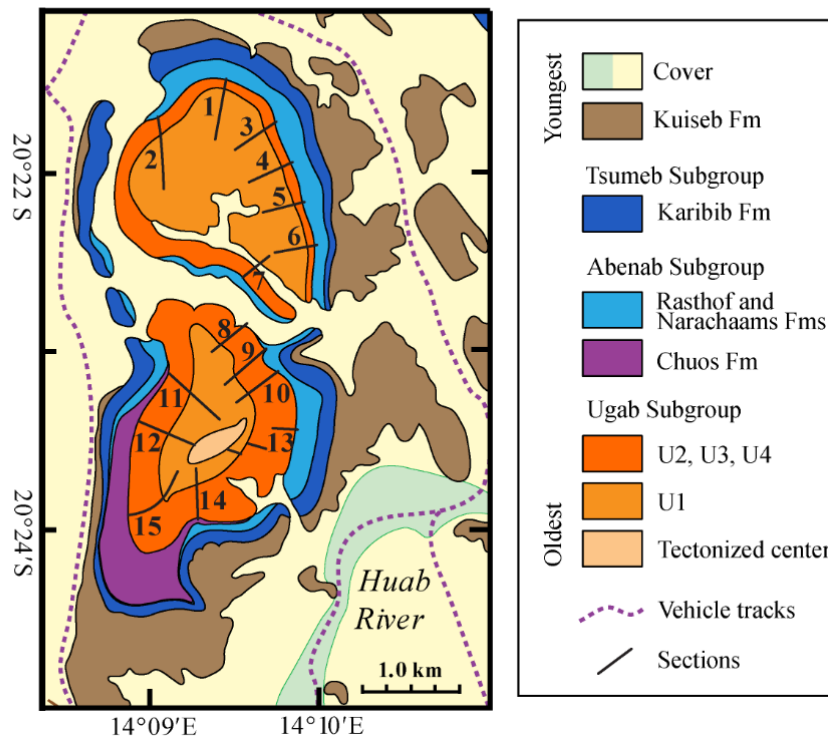
Figure 5: Geological map of the Vrede Domes with measured section locations marked (see Figure 6 for corresponding sections). Modified from Hoffman et al. (2016). U1-4 are the subdivisions of the Ugab Subgroup as defined by Maloof (2000).

north to carbonate-dominated strata in the south. The South Dome exposes the Ugab strata up to a greater depth than the North Dome with a highly tectonized carbonate at the base. It is unknown if the Naauwpoort Formation lies beneath, or if the Ugab Subgroup here lies directly on Paleoproterozoic basement.

The Chuos Formation is not laterally continuous in the Vrede Domes and mainly overlies the Ugab Subgroup in the southern end of the South Dome (***Figure 5***), where it appears as a thick wedge interpreted as a moraine-like deposit due to the stratigraphic onlap of overlying strata and absence of significant incision into the underlying Ugab Subgroup (Hoffman et al., 2016; Hoffman et al., 2017). It also appears in some areas in the North Dome, where it is much thinner. Where the Chuos Formation is absent, the Rasthof Formation unconformably overlies the Ugab Subgroup.

268 *Ugab Subgroup Lithostratigraphy in the Vrede Domes*

269 Prior detailed stratigraphic logging and mapping in the Vrede Domes resulted in division of the Ugab

270 Subgroup into four unnamed units, referred to from lowermost to uppermost as U1, U2, U3, and U4.

271 These units were originally defined and described by Maloof (2000), divided by significant flooding

272 surfaces, and assigned to the Ombombo Subgroup, but later workers reassigned the strata to the Ugab

273 Subgroup while keeping the same divisions of units (Hoffman and Halverson, 2008; Hoffman et al.,

274 2016). Unit U1 only occurs in the South Dome, where it sits above the basal tectonized limestone. It

275 consists mainly of black to maroon limestones on the west side of the dome or dolostone on the east side,

276 and sandstones. The top of the unit shows a transition to coarse-grained polymictic conglomerate. Unit

277 U2 is made up of polymictic conglomerate, sandstone, and dolostone ribbonite, generally arranged in

278 fining-upwards cycles. However, the unit as whole coarsens upwards. In the North Dome, U2 is

279 dominated by coarse-grained conglomerate. A maximum age constraint of 743±10 Ma for the upper part

280 of U2 from U-Pb ages on detrital zircons (Nascimento et al., 2017; Hoffman and Halverson, 2018) is

281 consistent with the 746±2 Ma date from the Nauuwpoort Formation (Hoffman et al., 1996). The top of

282 U2 is defined by a flooding surface and U3 marks a transition to carbonate-dominated deposition. This

283 unit consists of shoaling upward cycles of dolostone ribbonites, *Tungussia*-type stromatolites, and

284 grainstones with silicified ooid beds containing individual ooids up to 0.5 cm in diameter. A major

285 flooding surface marks the base of U4, which comprises almost entirely dolostone ribbonite, usually in

286 beds that are decametres thick. Some sections include subordinate thin beds of grainstone or stromatolite.

287 The Ugab Subgroup is truncated and in places brecciated beneath the Sturtian subglacial erosive surface.

288 Correlation of U4 across the domes indicates variable depth of erosion on this boundary (*Figure 6*).

289 *Sequence Stratigraphic Architecture in the Vrede Domes*

290 Four fourth-order depositional sequences have been identified and divided into systems tracts in the

291 Vrede Domes (*Figure 6*). These depositional sequences (denoted in *Figure 6* as V1-V4) are different

292 from the units U1-U4 defined by Maloof (2000), and also distinct from the depositional sequences
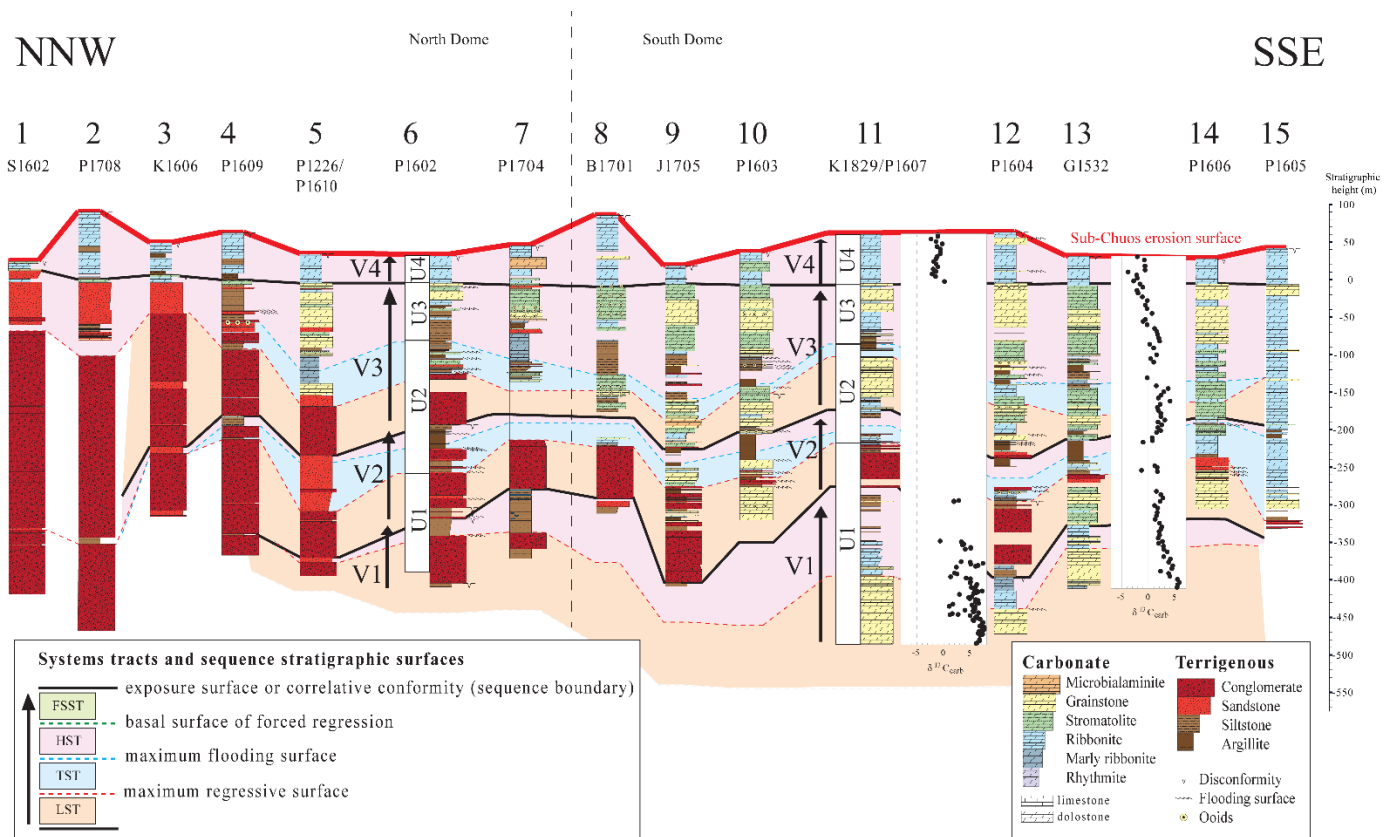
Figure 6: Stratigraphic sections of the Ugab Subgroup in the Vrede Domes, with base of uppermost

ribbonite unit (V4) as datum (Hoffman et al., 2017). Section locations are marked on Figure 5. V1-4 are

the depositional sequences described in text.

recognized in the Summas Mountains (S1-S4). The sequences show repeated abrupt increases in base

level, likely tectonically controlled, caused by slip on the extensional fault to the north of the Outjo basin.

The base of sequence V1 cannot be seen. In the North Dome, the lowest visible systems tract is an LST,

represented by a thick polymictic conglomerate unit, which grades laterally to a thick interval of

grainstone in the South Dome. No TST is preserved, and instead, a sharp flooding surface marks the base

of the overlying HST. The HST in the North Dome is represented by sandstone or siltstone, sometimes

containing carbonate concretions; ribbonite or marly ribbonite make up the HST in the South Dome.

An exposure surface, recognized in some sections by a scoured surface and discoloration of the

underlying siltstone, marks the base of sequence V2, followed by an LST generally consisting of over 50

306   metres of conglomerate in the North Dome. This thick conglomerate unit continues into the South Dome,

307   where it is variably interbedded with carbonates or finer-grained siliciclastics. A TST begins at the top of

308   the conglomeratic unit, ending with a maximum flooding surface near the base of an argillite unit. This is

309   followed by a thin HST represented by the argillite or fine siltstone unit, which can be traced across

310   nearly all the sections.

311   Sequence V3 begins, once again, with a thick conglomerate unit in the North Dome representing an LST.

312   In the South Dome, the LST consists of a few parasequences capped by stromatolite or grainstone. The

313   maximum regressive surface is generally found at the top of a thick grainstone unit, followed by a well-

314   developed TST recording fining upward. The base of the HST is another significant argillaceous unit,

315   containing several small-scale parasequences, that can be seen in nearly every section. Parasequence grain

316   size coarsens upwards and become dominated by stromatolite and ooid grainstone.

317   The base of sequence V4 is a significant flooding surface, marked by an abrupt transition to a ribbonite

318   unit, interpreted as an HST. It is erosionally truncated by the sub-Chuos glacial unconformity.

319   ***Carbon Isotope Results from the Vrede Domes***

320   Samples were collected from one full section (G1532) and two partial sections (K1829 and P1607) in the

321   South Dome of the Vrede Domes. Carbon isotope results from the Vrede Domes sections are plotted

322   stratigraphically in *Figure 6*, and show negligible correlation between δ^{13}C and δ^{18}O *(Figure 4)*. The full

323   section sampled on the east side of the South Dome (G1532) records a very gradual decline over nearly

324   450 metres of strata, from ~5 ‰ at the base of the section to a low around -3 ‰ at the top of the section.

325   The decline plateaus between 1 and 3 ‰ through the middle of the section. Section K1829, from the

326   western side of the South Dome, reproduces the beginning of the decline from baseline observed in the

327   lower part of G1532, but begins stratigraphically deeper. Section P1607, the uppermost ribbonite unit

328   roughly stratigraphically above K1829, reproduces the gradual decline into negative δ^{13}C values observed

329   at the top of the Ugab Subgroup in G1532.

16

330
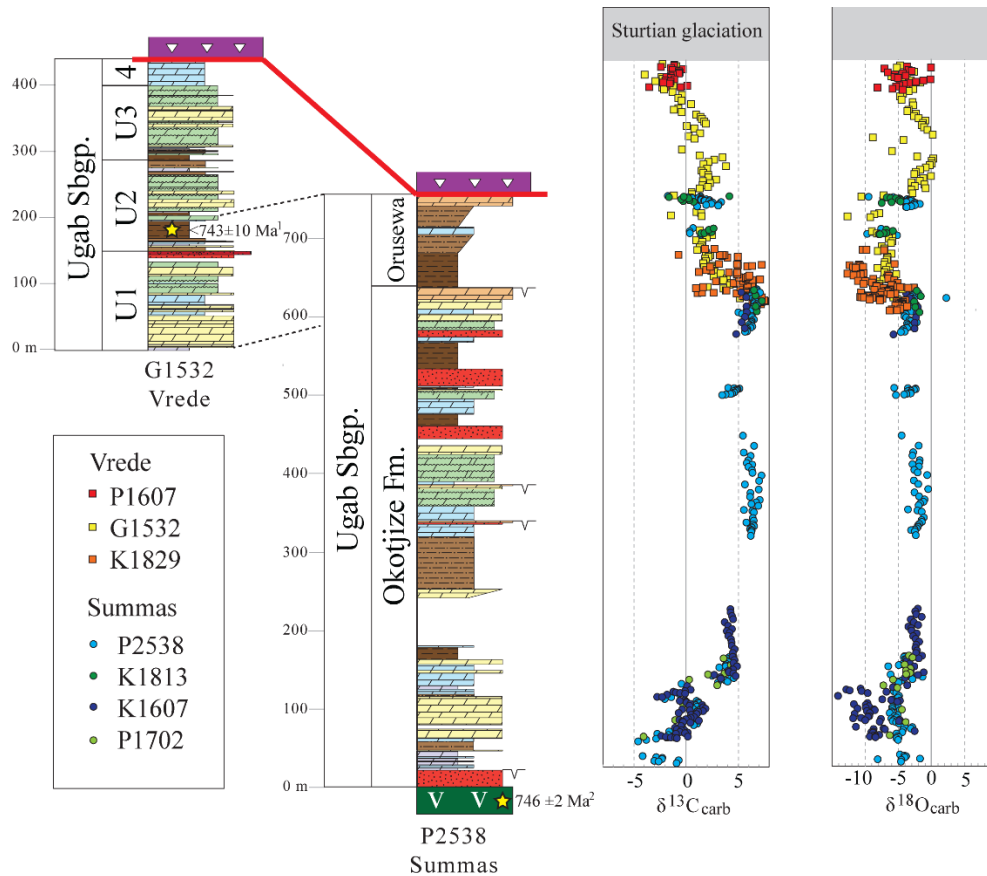
Figure 7: Composite carbon isotope profile of the Ugab Subgroup. Radiometric ages are from the

following references: 1: Nascimento et al., 2017; 2: Hoffman et al., 1996.

Discussion

Regional Correlations and a composite section

335   The $\delta^{13}C$ trends at the Vrede Domes and Summas Mountains are starkly different, suggesting that if the

336   trends are primary, the correlatable overlap between the two exposures of the Ugab Subgroup is relatively

337   small. Because the dominant control on base level fluctuation during the deposition of the Ugab Subgroup

338   in both the Summas Mountains and the Vrede Domes was local extension, which differed in each area,

339   the identified depositional sequences are of little to no use for correlation. Consequently, correlation

340   between the section sampled at the Vrede Domes and the sections from the Summas Mountains was made

341   based on the carbon isotope data and on the indication from available geochronology and

342   lithostratigraphic correlation of the overlying glacial deposits that the two regions broadly overlap in age.

343   The lower half of the Vrede Domes section records a descent from approximately 5‰ to 0‰ that can be

344   connected with a similar negative trend in the upper portion of the Summas Mountains section *(Figure 7)*.

345   The decline in δ^{13}C at the top of P2538 corresponds with scattered δ^{18}O declining to -10‰, which

346   suggests meteoric diagenesis may have been significant. However, the bulk of the δ^{18}O data lie between -

347   4 and -2‰, consistent with δ^{18}O values throughout most of the section, whereas all of the δ^{13}C data points

348   drop nearly 4‰ relative to the baseline. Though some of the samples were likely diagenetically driven

349   towards lower values, the decline in δ^{13}C at the top of P2538 cannot be explained by diagenesis alone.

350   The composite section covers a relatively complete record of the pre-Cryogenian in northwestern

351   Namibia, spanning nearly 1 km of strata unconformably lying between radiometrically dated volcanic

352   rocks giving a maximum age constraint for the base of 746±2 Ma (Hoffman et al., 1996), and the sub-

353   glacial erosion surface of the Sturtian glaciation, giving a maximum age constraint for the top of 717±0.2

354   Ma (Macdonald et al., 2010). This age-constrained profile can be used to propose global correlations.

355   *Late Tonian carbon isotope anomalies and global correlation*

356   Based on the proposed correlations between the two inliers, the Ugab Subgroup preserves two separate

357   negative δ^{13}C anomalies: an older one that is recorded at the base of the Summas Mountains sections, and

358   a younger one in the Vrede Domes. It is worth noting that this two-anomaly interpretation is made based

359   on the assumption that Fairchild et al (2018) were correct in their conclusion that the pre-Sturtian negative

360   anomaly recorded in Scotland lies immediately below conformable Sturtian glacial deposits, despite the

361   absence of age constraints within this succession that could validate this. Alternatively, the upper Ugab

362   Subgroup drop in δ^{13}C may represent a gradual decline in global seawater δ^{13}C preceding the glaciation,

363   rather than a truncated excursion.

364   Within the two-anomaly framework, we posit that the younger anomaly is truncated by sub-Chuos

365   erosion, where only the declining arm is preserved and the nadir and recovery have been removed. The

366   older excursion, near the base of the Summas Mountains sections, is much sharper and reaches more

367   negative values (ca. -4.5 ‰) than the Vrede Domes anomaly. However, it has a double-minima, which is

368   not observed in pre-Sturtian anomalies in other parts of the world. The association of the second

369   minimum with a flooding surface and subsequent deep-water facies suggests that it could be a secondary

370   feature resulting from authigenic carbonate contribution or alteration, but we also explore the possibility

371   that it is a primary seawater signal.

372   In the context of the recently updated δ^{13}C record from Scotland (Fairchild et al., 2018), our data set is

373   consistent with the existence of at least two separate global negative carbon isotope anomalies recorded in

374   marine carbonates deposited between the ca. 802 Ma end of the Bitter Springs anomaly and the onset of

375   the Sturtian glaciation (Fairchild et al., 2018; Halverson et al., 2018a). To avoid confusion, in this

376   discussion we will use the convention of Halverson et al. (2018b) of referring to the older of the two

377   anomalies (ca. 735 Ma) as the Russøya anomaly following Halverson et al. (2004), and the younger (ca.

378   720 Ma) as the Garvellach anomaly following Fairchild et al. (2018). We interpret the negative excursion

379   at the base of the Summas Mountains sections as the Russøya anomaly and the decline in δ^{13}C observed

380   in the Vrede Domes as the Garvellach anomaly, with the nadir and recovery erosionally severed. The

381   protracted expression of the decline in δ^{13}C in the upper Ugab Subgroup seems inconsistent with the

382   Garvellach anomaly in Scotland, however that may be explained by the differences in sedimentation rates

383   between the Ugab Subgroup in the Vrede Domes, where subsidence was fault-driven during active rifting,

384   and the uppermost Appin Group in the Garvellach Islands.

385   The maximum age constraint of ca. 746 Ma for the base of the Ugab Subgroup in the Summas Mountains

386   (Hoffman et al., 1996) is consistent with a ca. 735 Ma age for the Russøya anomaly (MacLennan et al.,

387   2018) and effectively rules out the possibility of correlation with the Bitter Springs anomaly. It is very

388   likely that strata recording the immediately pre-glacial Garvellach anomaly have been removed in many

389   regions by erosive scour beneath the glacial surface. In areas where the Garvellach anomaly has not been

390   removed, the older Russøya anomaly could be mistaken for the ca. 810-802 Ma Bitter Springs anomaly in

391   successions with few or no age constraints. This complicates using late Tonian anomalies as

392   chronostratigraphic markers, because in sections preserving only one pre-Sturtian negative anomaly, it

393   may difficult to ascertain which of the two excursions is preserved. On the other hand, whereas both the

394   Russøya and Garvellach anomalies appear to define a sharp minimum, the Bitter Springs anomaly is

395   distinguished by a plateau of low δ^{13}C values that likely spanned millions of years (Halverson et al.,

396   2018b).

397
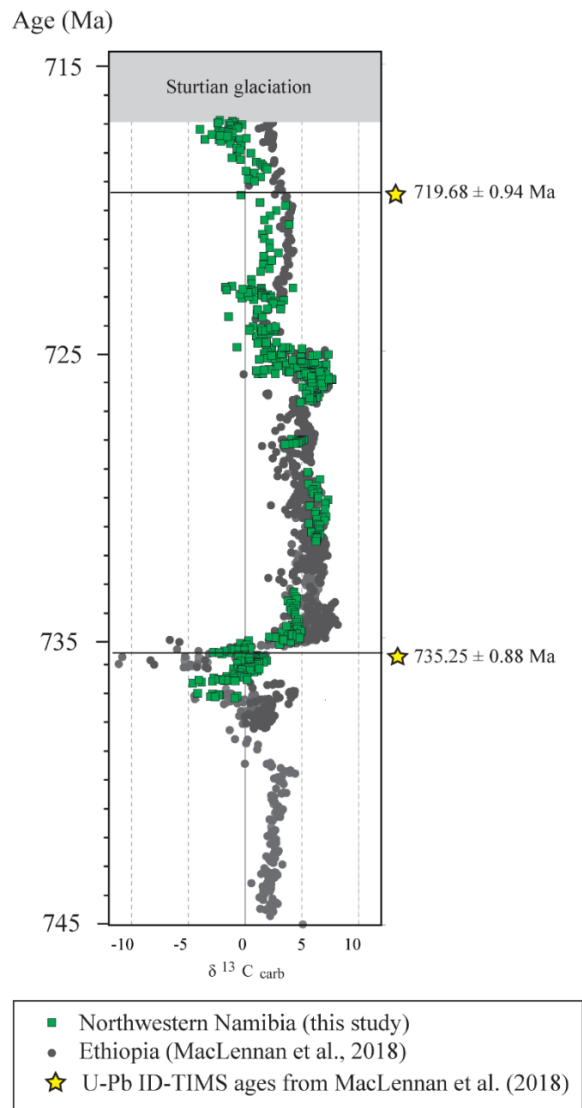
398   *Figure 8: Ugab Subgroup δ^{13}C profile superimposed on upper Tambien Group δ^{13}C profile with U-Pb*

399   *ID-TIMS dates and age model (MacLennan et al., 2018).*

400   The carbon isotope record of the uppermost ~700 metres of the Tambien Group in Ethiopia is notably

401   similar to that of the Ugab Subgroup, with a sharper anomaly and return to baseline several hundreds of

402   metres beneath glaciogenic deposits, followed by a gradual decline in the hundreds of metres immediately

403   below the sub-glacial unconformity (Swanson-Hysell et al., 2015; MacLennan et al., 2018). The onset of

404   this upper decline coincides with a shift to deposition of dominantly deeper-water facies, which could

405   suggest this trend may be related to authigenic carbonate contribution. However, our data shows a similar

406   upper decline with seemingly no facies dependence. Therefore, we tentatively suggest that the Ugab

407   Subgroup strata exposed in the Vrede Domes may be correlative with the Mariam Bohkakho Formation

408   of the Tambien Group of Ethiopia (*Figure 8*). Correlation of U-Pb radiometric ages into the Ugab

409   composite δ^{13}C section suggest that upper Ugab Subgroup in the Vrede Domes preserves a very complete,

410   immediately pre-Sturtian stratigraphic record.

411   **Conclusions**

412   The Ugab Subgroup in the Northern Margin Zone of Namibia preserves a latest Tonian, pre-Sturtian

413   stratigraphic record. We demonstrate that this record preserves evidence of two distinct negative carbon

414   isotope excursions between ca. 746–717 Ma. This result is consistent with recent data and interpretation

415   suggesting that there were two separate global δ^{13}C excursions prior to the onset of Cryogenian glaciation,

416   ca. 735 and ca. 718 Ma (Halverson et al. 2018; MacLennan et al., 2018). This result has important

417   implications for correlating between Tonian successions and for formally defining the base of the

418   Cryogenian period, which will likely be linked to chemostratigraphic records (Shields-Zhou et al., 2016).

419   Furthermore, the data presented here will aid with the construction of a robust, age-calibrated pre-

420   Cryogenian carbon isotope record, which is essential to understanding the factors that led to the first

421   Cryogenian Snowball Earth. If the younger pre-Sturtian δ^{13}C anomaly does indeed record a global

422   seawater signal, then it, rather than the better defined Russøya anomaly, is likely to be mechanistically

423   linked to the Sturtian glaciation.

424   **Acknowledgements**

430

References

432 Ali, D.O., Spencer, A.M., Fairchild, I.J., Chew, K.J., Anderton, R., Levell, B.K., Hambrey, M.J., Dove,

433 D., Le Heron, D.P., 2018. Indicators of relative completeness of the glacial record of the Port Askaig

434 Formation, Garvellach Islands, Scotland. Precambrian Res. 319, 65-78.

435 Allan, J.R. and Matthews, R.K., 1982. Isotope signatures associated with early meteoric diagenesis.

436 Sedimentology, 29(6), pp.797-817.

437 Fairchild, I.J., Spencer, A.M., Ali, D.O., Anderson, R.P., Anderton, R., Boomer, I., Dove, D., Evans, J.D.,

438 Hambrey, M.J., Howe, J. and Sawaki, Y., 2018. Tonian-Cryogenian boundary sections of Argyll,

439 Scotland. Precambrian Res. 319, 37-64.

440 Guj, P. and Kröner, A., 1974. A revision of the Damara stratigraphy along the southern margin of the

441 Kamanjab inlier, South West Africa. Contributions to the Precambrian Geology of Southern Africa:

442 University of Cape Town Precambrian Research Unit Bulletin, 15, pp.167-176.

443 Halverson, G.P., Hoffman, P.F., Schrag, D.P., Kaufman, A.J., 2002. A major perturbation of the carbon

444 cycle before the Ghaub glaciation (Neoproterozoic) in Namibia: Prelude to snowball Earth? Geochem.

445 Geophys. Geosystems 3, 1–24.

446 Halverson, G.P., Hoffman, P.F., Schrag, D.P., Maloof, A.C., Rice, A.H.N., 2005. Toward a

447 Neoproterozoic composite carbon-isotope record. Geol. Soc. Am. Bull. 117, 1181–1207.

448   Halverson, G.P. and Shields-Zhou, G., 2011. Chemostratigraphy and the Neoproterozoic glaciations.

449   Geological Society, London, Memoirs, 36(1), pp.51-66.

450   Halverson, G.P., Porter, S.M. and Gibson, T.M., 2018a. Dating the late Proterozoic stratigraphic record.

451   Emerging Topics in Life Sciences, 2(2), pp.137-147.

452   Halverson, G.P., Kunzmann, M., Strauss, J.V. and Maloof, A.C., 2018b. The Tonian-Cryogenian

453   transition in Northeastern Svalbard. Precambrian Res. 319, 79-95.

454   Henry, G., Clendenin, C.W., Stanistreet, I.G. and Maiden, K.J., 1990. Multiple detachment model for the

455   early rifting stage of the Late Proterozoic Damara orogen in Namibia. Geology, 18(1), pp.67-71.

456   Hoffman, P.F., 1991. Did the breakout of Laurentia turn Gondwanaland inside-out. Science 252, 1409–

457   1412.

458   Hoffman, P.F., Hawkins, D.P., Isachsen, C.E. and Bowring, S.A., 1996. Precise U–Pb zircon ages for

459   early Damaran magmatism in the Summas Mountains and Welwitschia Inlier, northern Damara belt,

460   Namibia. Comm. Geol. Surv. Namibia, 11, pp.47-52.

461   Hoffman, P.F., Kaufman, A.J., Halverson, G.P., Schrag, D.P., 1998a. A Neoproterozoic snowball earth.

462   Science 281, 1342–1346.

463   Hoffman, P.F., 1999. The break-up of Rodinia, birth of Gondwana, true polar wander and the snowball

464   Earth. J. Afr. Earth Sci. 28, 17–33.

465   Hoffman, P. and Halverson, G., 2008. 'Otavi Group of the Western Northern Platform, the Eastern Kaoko

466   Zone and the Western Northern Margin Zone' in the Geology of Namibia. Windhoek Namib. Minist.

467   Mines Energy Geol. Surv., pp. 13-69 – 13-126.

468   Hoffman, P.F., Halverson, G.P., Domack, E.W., Maloof, A.C., Swanson-Hysell, N.L., Cox, G.M., 2012.

469   Cryogenian glaciations on the southern tropical paleomargin of Laurentia (NE Svalbard and East

470 Greenland), and a primary origin for the upper Russøya (Islay) carbon isotope excursion. Precambrian

471 Res. 206, 137–158.

472 Hoffman, P.F., Bellefroid, E.J., Crockford, P.W., de Moor, A., Halverson, G.P., Hodgin, E.B., Hodgskiss,

473 M.S.W., Holtzman, B.K., Jasechko, G.R., Johnson, B.W. and Lamothe, K.G., 2016. A misfit Cryogenian

474 diamictite in the Vrede domes, Northern Damara Zone, Namibia: Chuos (Sturtian) or Ghaub (Marinoan)

475 Formation? Moraine or paleovalley. Commun. Geol. Surv. Namibia, 17, pp.1-16.

476 Hoffman, P.F., Lamothe, K.G., LoBianco, S.J., Hodgskiss, M.S., Bellefroid, E.J., Johnson, B.W., Hodgin,

477 E.B. and Halverson, G.P., 2017. Sedimentary depocenters on Snowball Earth: Case studies from the

478 Sturtian Chuos Formation in northern Namibia. Geosphere, 13(3), pp.811-837.

479 Hoffman, P.F. and Halverson, G.P., 2018. Discussion of "Depositional ages and provenance of the

480 Neoproterozoic Damara Supergroup (northwest Namibia): Implications for the Angola–Congo and

481 Kalahari cratons connection" by Débora B. Nascimento, Renata S. Schmitt, André Ribeiro, Rudolph AJ

482 Trouw, Cees W. Passchier, and Miguel AS Basei. Gondwana Research.

483 Hoffman, P.F., Lamothe, K.G. & Greenman, J.W., 2018. Report: Stratigraphic investigations of the

484 Neoproterozoic Otavi/Swakop Group in the southern Kunene Region. Communications of the Geological

485 Survey of Namibia, 20, 100-113.

486 Kirschvink, J.L., 1992. Late Proterozoic low-latitude global glaciation: the snowball earth. In: Schopf,

487 J.W., Klein, C. (Eds.), The Proterozoic Biosphere. Cambridge University Press, pp. 51–52.

488 Knoll, A.H., Walter, M.R., Narbonne, G.M. and Christie-Blick, N., 2004. A new period for the geologic

489 time scale. Science, 305 (5684), pp.621-622.

490 Krapez, B., 1996. Sequence stratigraphic concepts applied to the identification of basin-filling rhythms in

491 Precambrian successions. Australian Journal of Earth Sciences, 43(4), pp.355-380.

492   McKirdy, D.M., Burgess, J.M., Lemon, N.M., Yu, X., Cooper, A.M., Gostin, V.A., Jenkins, R.J. and

493   Both, R.A., 2001. A chemostratigraphic overview of the late Cryogenian interglacial sequence in the

494   Adelaide Fold-Thrust Belt, South Australia. Precambrian Research, 106(1-2), pp.149-186.

495   Meert, J.G., Lieberman, B.S., 2008. The Neoproterozoic assembly of Gondwana and its relationship to

496   the Ediacaran–Cambrian radiation. Gondwana Res. 14, 5–21.

497   Macdonald, F.A., Schmitz, M.D., Crowley, J.L., Roots, C.F., Jones, D.S., Maloof, A.C., Strauss, J.V.,

498   Cohen, P.A., Johnston, D.T., Schrag, D.P., 2010a. Calibrating the Cryogenian. Science 327, 1241–1243.

499   Macdonald, F.A., Schmitz, M.D., Strauss, J.V., Halverson, G.P., Gibson, T.M., Eyster, A., Cox, G.,

500   Mamrol, P. and Crowley, J.L., 2018. Cryogenian of Yukon. Precambrian Res. 319, 114-143.

501   MacLennan, S., Park, Y., Swanson-Hysell, N., Maloof, A., Schoene, B., Gebreslassie, M., Antilla, E.,

502   Tesema, T., Alene, M. and Haileab, B., 2018. The arc of the Snowball: U-Pb dates constrain the Islay

503   anomaly and the initiation of the Sturtian glaciation. Geology, 46(6), pp.539-542.

504   Maloof, A.C., 2000. Superposed folding at the junction of the inland and coastal belts, Damara Orogen,

505   NW Namibia. Communications of the Geological Survey of Namibia, 12, pp.89-98.

506   Miller, R.M., 2008. The geology of Namibia. Neoproterozoic Low. Palaeoz. Windhoek Namib. Minist.

507   Mines Energy Geol. Surv.

508   Miller, R.M., 1983. The Pan-African Damara Orogen of South West Africa/Namibia. Geol. Soc. S. Afr.

509   Spec. Publ., 11: 431-515. Miller, R.M., 1980. Geology of a portion of central Damaraland, South West

510   Africa/Namibia. Memoirs of the Geological Survey of SW Africa/Namibia, 6, pp.1-78.

511   Miller, R.M., 1974. The stratigraphic significance of the Naauwpoort Formation of east central

512   Damaraland, South West Africa. South African Journal of Geology, 77(3), pp.363-367.

513   Nascimento, D.B., Schmitt, R.S., Ribeiro, A., Trouw, R.A., Passchier, C.W. and Basei, M.A., 2017.

514   Depositional ages and provenance of the Neoproterozoic Damara Supergroup (northwest Namibia):

Implications for the Angola-Congo and Kalahari cratons connection. Gondwana Research, 52, pp.153-171.

Pisarevsky, S.A., Wingate, M.T., Powell, C.M., Johnson, S., Evans, D.A., 2003. Models of Rodinia assembly and fragmentation. Geol. Soc. Lond. Spec. Publ. 206, 35–55.

Porter, S.M., 2004. The fossil record of early eukaryotic diversification. Paleontol. Soc. Pap. 10, 35.

Pu, J.P., Bowring, S.A., Ramezani, J., Myrow, P., Raub, T.D., Landing, E., Mills, A., Hodgin, E., Macdonald, F.A., 2016. Dodging snowballs: Geochronology of the Gaskiers glaciation and the first appearance of the Ediacaran biota. Geology 44, 955–958.

Rooney, A.D., Macdonald, F.A., Strauss, J.V., Dudás, F.Ö., Hallmann, C., Selby, D., 2014. Re-Os geochronology and coupled Os-Sr isotope constraints on the Sturtian snowball Earth. Proc. Natl. Acad. Sci. 111, 51–56.

Shields-Zhou, G.A., Porter, S., Halverson, G.P., 2016. A new rock-based definition for the Cryogenian Period (circa 720-635 Ma). Episodes 39, 3–8.

Shields, G.A., Halverson, G.P. and Porter, S.M., 2018. Descent into the Cryogenian. Precambrian Res. 319, 1-5.

Strauss, J.V., Rooney, A.D., Macdonald, F.A., Brandon, A.D., Knoll, A.H., 2014. 740 Ma vase-shaped microfossils from Yukon, Canada: Implications for Neoproterozoic chronology and biostratigraphy. Geology 42, 659–662.

Strauss, J.V., MacDonald, F.A., Halverson, G.P., Tosca, N.J., Schrag, D.P., Knoll, A.H., 2015. Stratigraphic evolution of the Neoproterozoic Callison Lake Formation: Linking the break-up of Rodinia to the Islay carbon isotope excursion. Am. J. Sci. 315, 881–944.

536 Swanson-Hysell, N.L., Maloof, A.C., Condon, D.J., Jenkin, G.R., Alene, M., Tremblay, M.M., Tesema,

537 T., Rooney, A.D., Haileab, B., 2015. Stratigraphy and geochronology of the Tambien Group, Ethiopia:

538 Evidence for globally synchronous carbon isotope change in the Neoproterozoic. Geology 43, 323–326.

539 **Supplementary**

540 Supplementary Table 1: Facies descriptions, from Hoffman and Halverson (2008).

	Facies	Description	Depositional environment
Shallowest	Microbialaminite	Thinly laminated carbonate sediments with crinkly lamination. May have sedimentary structures that suggest a shallow depositional environment such as teepee structures and breccias.	Intertidal to supratidal zones
	Grainstone	Carbonate sands. Often display dark-coloured silicification, likely due to the high primary permeability, which occasionally preserves giant ooids and crossbedding	Sub- to lower intertidal zone, under continual influence of wave break action
Shoaling	Stromatolite	Mounded microbial growth structures, often Tungussia-type - columnar stromatolites with divergent branching patterns, and pinkish in colour. Conophyton-type stromatolites may also be present.	Sub-tidal zone, maximum depth limited by photic zone
	Ribbonite	Finely laminated silt-to-fine-sand -sized carbonate sediments showing low-angle cross-stratification. May be mixed with siliciclastic muds (marly ribbonite).	Low-energy zone well below breaking waves but above the storm wave base
Deepest	Rhythmite	Parallel-laminated carbonate muds, may also contain turbidites.	Below storm wave base

541

542 Supplementary Table 2: Coordinates at bases of sampled sections.

Section	Coordinates at base	Location
K1813	S20°29.960' E015°19.388'	Loewenfontein
P1702	S20°29.604' E015°19.330'	Loewenfontein
K1607	S20°28.557' E015°19.950'	Rondehoek
K1829	S20°23.549' E014°09.417'	Vrede
G1532	S20°23'35.4" E014°09'30.2"	Vrede
P1607	S20°23'16.8" E014°09'04.0"	Vrede

543

544 Supplementary Table 3: Carbon and oxygen isotope data and composite section heights. Section location

545 information provided in Table 2.

K1607			
sample height (m)	composite height (m)	$\delta^{13}C$ (‰)	$\delta^{18}O$ (‰)
332.9	618.5	5.36	-3.87
330.3	612.3	5.86	-3.32
325.5	600.9	5.88	-2.06
322.5	593.8	5.91	-2.20
320	587.9	5.73	-2.35
317.2	581.2	5.40	-2.55
314.1	573.9	5.71	-2.55
311	566.5	4.86	-5.78
248.8	221.8	4.29	-2.06
245.8	218.4	4.30	-2.45
242.4	214.6	4.44	-2.31
239.5	211.4	4.55	-1.46
236.7	208.3	3.72	-3.14
233.4	204.6	4.05	-2.66
230.4	201.2	4.44	-2.00
228.5	199.1	3.93	-3.51
226.8	197.2	4.21	-3.06
224	194.1	4.08	-3.02
220.9	190.6	4.34	-2.22

217.9	187.2	4.40	-2.77
214.8	183.8	4.42	-2.39
211.6	180.2	4.70	-1.84
208.2	176.4	4.52	-2.31
204.6	172.4	4.52	-2.42
201.7	169.1	4.69	-2.19
198.9	166.0	4.59	-2.34
195.8	162.5	4.94	-1.41
192.8	159.2	4.56	-1.91
190	156.0	4.07	-3.76
186.9	152.6	4.13	-3.27
183.8	149.1	4.57	-2.58
180.1	145.0	2.68	-3.08
177.2	141.7	4.81	-1.16
174.2	138.4	3.26	-2.04
171	134.8	3.33	-4.03
152.8	125.4	0.00	-3.67
143.9	123.0	0.35	-5.85
136.8	121.2	-0.21	-10.80
132.7	120.1	-1.37	-12.99
128.2	118.9	-1.12	-12.47
125.2	118.1	-0.70	-10.65
122	117.2	-0.20	-6.86
115.9	115.6	-1.99	-9.72
103	112.2	-2.97	-14.26

101.8	111.9	-2.47	-14.24
93.5	107.7	-0.24	-7.49
92.2	106.9	-0.73	-6.13
90.8	106.0	-0.09	-4.79
88.8	104.7	-0.07	-5.18
86.1	103.0	0.32	-9.75
84	101.7	1.49	-11.83
82.5	100.8	0.24	-10.01
79.6	99.0	1.59	-9.54
76.7	97.1	1.82	-10.01
75.1	96.1	-0.49	-11.27
73.4	95.1	0.27	-8.75
71.8	94.1	1.57	-8.63
70.1	93.0	1.11	-9.85
68.2	91.8	-0.84	-18.51
66	90.4	0.94	-9.40
64.4	89.4	0.39	-11.73
59.9	86.6	0.69	-9.47
58.5	85.7	0.36	-9.68
56.4	84.4	0.10	-10.74
55.6	83.9	-0.14	-11.95
54.3	83.1	-0.77	-7.69
52.8	82.1	1.16	-4.85
51.6	81.4	-0.48	-10.10
50.2	80.5	-0.40	-4.96

sample height (m)	composite height (m)	δ¹³C (‰)	δ¹⁸O (‰)
48.8	79.6	0.32	-7.89
42.3	75.5	-0.61	-15.81
38.6	73.2	-1.20	-11.52
35.5	71.2	-1.03	-7.30
34.2	70.4	-0.29	-8.82
33.6	70.0	-0.57	-7.08
30.1	67.8	-0.71	-2.54
29.1	67.2	0.06	-8.84
27.8	66.4	-0.21	-9.16
26.8	65.8	-1.11	-8.91
22.4	63.0	-2.55	-7.96
21.2	62.2	0.07	-8.57
20.6	61.9	-2.11	-8.90
19.3	61.0	-1.62	-9.40
18.7	60.7	-1.18	-8.59
17.8	60.1	-1.02	-8.52
G1532			
sample height (m)	composite height (m)	$\delta^{13}C$ (‰)	$\delta^{18}O$ (‰)
440.3	904.9	-2.19	-4.76
436	902.0	-0.84	-5.24
428	896.7	-0.73	-2.58
422.6	893.0	-0.72	-3.76
420	891.3	-3.97	-6.08
416	888.6	-2.31	-4.27
412	885.9	-2.20	-3.14

408	883.3	-2.90	-1.66
404	880.6	-1.68	-2.77
399.9	877.8	-1.15	-3.53
395.5	874.9	-2.26	-2.74
392	872.5	-2.06	-3.47
387	869.2	-1.23	-4.31
382	865.8	-0.28	-4.79
376	861.8	-0.66	-4.54
371.3	858.7	-0.33	-2.85
365	854.5	0.62	-2.75
356.9	849.0	-0.65	-3.48
354.4	847.4	-1.09	-3.66
350	844.4	-0.31	-2.33
345	841.1	1.11	-2.63
341	838.4	1.53	-1.92
336.9	835.6	1.68	-0.91
332.1	832.4	1.92	-1.28
328.2	829.8	2.07	-1.46
324	827.0	0.18	-1.10
319.2	823.8	0.93	-0.58
310.1	817.7	1.50	0.23
304.9	814.2	0.38	-8.92
300.3	811.1	0.95	-4.26
279.5	797.2	-0.29	-6.02
268.9	790.1	1.44	-2.16

265.3	787.7	3.72	0.30
261	784.8	2.89	0.04
256.4	781.7	2.33	0.06
252.7	779.2	1.83	-0.22
248.6	776.5	4.06	-0.83
244.3	773.6	2.19	-1.71
240.2	770.9	1.64	-2.38
236.3	768.2	1.81	-2.58
232.4	765.6	2.30	-0.05
228	762.7	2.32	-1.22
223.5	759.7	3.08	-1.76
220.7	757.8	1.77	-3.03
217	755.3	2.48	-1.06
213.3	752.8	1.73	-2.53
209.6	750.4	2.28	-0.86
207	748.6	1.48	-3.07
200	743.9	0.66	-2.85
196.2	741.4	0.69	-7.29
194	739.9	-1.09	-10.68
162.8	719.0	1.15	-7.94
160.6	717.5	1.60	-8.70
156.7	714.9	-1.39	-12.81
155.1	713.9	1.65	-9.34
128.8	696.2	1.46	-9.08
124.5	693.4	2.31	-8.31

120	690.3	2.71	-5.97
115.5	687.3	2.17	-6.50
110	683.6	1.11	-5.92
106.5	681.3	1.72	-6.15
100.7	677.4	1.61	-7.59
96.5	674.6	1.47	-7.18
91.7	671.4	1.23	-8.18
86.6	668.0	2.06	-6.07
81.6	664.6	2.49	-6.75
78.8	662.7	2.34	-6.69
75.3	660.4	1.97	-6.81
70.6	657.3	2.07	-7.10
66.7	654.6	1.80	-7.19
62.3	651.7	2.61	-6.35
59.7	650.0	1.89	-8.24
56	647.5	2.80	-6.92
51.5	644.5	2.90	-7.18
48.4	642.4	3.54	-5.36
42.2	638.2	2.85	-6.83
38.9	636.0	4.14	-7.30
34.8	633.3	3.81	-8.30
30	630.1	4.58	-7.91
26.2	627.5	4.42	-8.88
22.7	625.2	2.25	-2.64
19.8	623.2	3.80	-4.39

sample height (m)	composite height (m)	δ13C (‰)	δ18O (‰)
16	620.7	4.02	-7.35
12	618.0	5.48	-6.02
7.8	615.2	5.87	-5.82
4.6	613.0	5.50	-5.79
1.4	610.9	5.42	-5.19
P1607			
sample height (m)	composite height (m)	$\delta^{13}C$ (‰)	$\delta^{18}O$ (‰)
88.8	903.3	-1.15	-3.74
85.5	902.2	-1.18	-0.05
81	900.7	-2.45	-7.14
76.5	899.2	-1.49	-3.46
72.3	897.8	-0.31	-2.96
67.5	896.2	-1.32	-6.63
63	894.7	-0.71	-4.35
58.5	893.3	-0.64	-5.54
54.1	891.8	-0.71	-3.90
49.5	890.3	-1.29	-5.63
45	888.8	-1.51	-5.08
40.5	887.3	-1.94	-0.10
36	885.8	-1.50	-1.22
31.5	884.3	-1.35	-2.34
26.9	882.8	-2.04	-3.43
22.5	881.3	-1.52	-4.16
18	879.8	-2.24	-4.86
13.5	878.3	-1.59	-5.39

9	876.9	-1.01	-8.19
4.6	875.4	0.10	-5.91
0.4	874.0	-0.61	-4.36
K1829			
sample height (m)	composite height (m)	$\delta^{13}C$ (‰)	$\delta^{18}O$ (‰)
237.8	673.0	2.89	-10.54
236.9	672.7	1.98	-9.91
235.9	672.4	1.97	-7.22
182.0	655.0	-0.66	-5.62
180.5	654.5	3.38	-11.03
178.0	653.7	3.69	-12.51
176.5	653.2	3.87	-11.11
175.0	652.8	3.62	-10.85
170.8	651.4	5.18	-10.42
169.3	650.9	5.16	-11.97
167.7	650.4	4.14	-11.55
145.3	643.2	3.34	-10.37
144.6	643.0	5.09	-12.82
142.5	642.3	7.53	-10.79
141.0	641.8	5.19	-6.68
138.9	641.1	6.58	-11.42
137.3	640.6	6.11	-11.88
135.7	640.1	2.45	-6.49
125.3	636.7	2.08	-6.57
123.8	636.3	2.57	-8.86

118.8	634.7	1.34	-5.66
116.5	633.9	4.31	-11.21
115.3	633.5	5.12	-10.11
109.6	631.7	5.14	-9.05
108.1	631.2	5.08	-5.15
105.1	630.2	6.33	-10.36
101.7	629.1	6.15	-5.96
100.1	628.6	5.29	-6.06
98.7	628.2	5.62	-8.43
97.0	627.6	6.01	-8.01
95.1	627.0	5.96	-8.35
93.6	626.5	7.36	-5.12
92.3	626.1	6.17	-4.57
92.3	626.1	6.61	-4.8
90.8	625.6	6.24	-2.69
89.2	625.1	5.71	-3.52
87.6	624.6	3.02	-7.29
83.4	623.2	5.37	-6.33
81.8	622.7	4.78	-8.69
79.9	622.1	4.99	-6.31
78.4	621.6	6.14	-6.82
76.8	621.1	6.58	-7.09
74.8	620.5	6.04	-6.3
73.4	620.0	6.27	-6.64
71.9	619.5	6.67	-7.54

70.4	619.1	1.77	-10.74
68.9	618.6	5.42	-5.82
66.5	617.8	1.07	-5.51
65.6	617.5	5.97	-6.71
64.1	617.0	5.71	-6.25
62.6	616.5	5.92	-7.77
61.1	616.1	5.96	-7.78
59.6	615.6	4.07	-9.58
58.1	615.1	5.64	-8.82
56.6	614.6	5.74	-9.4
55.1	614.1	6.66	-8.61
53.6	613.6	1.66	-10.86
52.1	613.2	2.78	-10.69
51.6	613.0	1.22	-10.32
50.1	612.5	5.06	-8.94
48.6	612.0	6.37	-7.96
47.1	611.6	6.11	-9.38
45.6	611.1	6.52	-7.46
44.1	610.6	6.96	-7.82
42.6	610.1	5.57	-9.43
41.0	609.6	5.76	-7.87
39.5	609.1	8.57	-3.94
38.0	608.6	7.52	-5.09
36.4	608.1	7.36	-5.32
34.9	607.6	7.33	-4.35

33.4	607.1	7.34	-4.3
31.6	606.6	6.9	-5.09
29.3	605.8	7.8	-4.62
27.7	605.3	7.73	-4.41
26.2	604.8	7.86	-4.91
24.6	604.3	7.33	-4.48
23.1	603.8	7.49	-4.49
21.6	603.3	6.75	-5.14
20.1	602.9	6.85	-4.9
18.6	602.4	6.6	-5.49
17.0	601.9	7.44	-4.1
15.6	601.4	6.98	-3.7
7.6	598.8	6.85	-4.73
5.4	598.1	6.85	-6.05
1.7	596.9	6.38	-5.23
0.7	596.6	6.21	-6.37
K1813			
sample height (m)	composite height (m)	$\delta^{13}C$ (‰)	$\delta^{18}O$ (‰)
229.9	738.7	-0.38	-6.8
229.3	738.1	-0.26	-6.22
228.7	737.6	-1.7	-5.43
227.1	736.0	0.22	-4.72
226.1	735.1	-0.51	-4.95
224.7	733.7	0.29	-4.7
223.6	732.7	-0.32	-6.07

sample height (m)	composite height (m)	$\delta^{13}C$ (‰)	$\delta^{18}O$ (‰)
222.7	731.8	0.71	-7.58
183	698.4	2.72	-6.88
181.2	696.7	2.26	-5.86
178.3	693.9	2.54	-6.85
178.1	693.7	2.36	-7.28
176.9	692.6	1.83	-8.04
176.7	692.4	1.5	-7.85
80.2	621.5	6.57	-2.23
69.6	614.6	6.72	-1.60
59.1	607.7	7.35	-2.62
48.6	600.9	6.74	-2.45
38.7	594.4	6.85	-1.8
P1702			
sample height (m)	composite height (m)	$\delta^{13}C$ (‰)	$\delta^{18}O$ (‰)
132.3	162.7	4.58	-3.42
128.9	160.3	3.59	-2.86
116.1	151.5	4.32	-4.07
109.3	146.8	4.52	-3.20
105	143.8	4.53	-3.88
100.9	141.0	3.69	-3.23
98.6	139.4	2.04	-3.83
88.8	132.6	0.17	-5.85
78.3	125.3	2.96	-7.32
72	122.3	-0.11	-5.18
68.5	94.8	-0.41	-4.49

66.5	79.1	-1.22	-3.91
64.4	62.6	-4.37	-6.35
P2538			
	composite height (m)	$\delta^{13}C$ (‰)	$\delta^{18}O$ (‰)
	739.6	-1.89	-9.58
	739.2	1.34	-5.82
	738.7	1.35	-6.44
	738.2	0.13	-7.30
	737.8	0.47	-7.36
	737.5	1.17	-4.91
	737.0	0.49	-4.76
	736.6	1.37	-3.69
	736.1	1.44	-3.39
	735.7	1.40	-3.01
	735.3	1.92	-3.43
	734.9	1.37	-3.28
	734.6	1.43	-3.24
	734.3	2.23	-3.13
	733.7	1.70	-4.02
	733.3	1.76	-3.94
	732.9	2.21	-3.80
	732.0	3.39	-2.42
	731.4	2.55	-2.60
	730.6	2.34	-1.74
	729.8	2.42	-2.75

	729.0	3.14	-2.51
	728.3	1.90	-3.16
	727.5	3.10	-3.06
	727.0	0.99	-3.88
	726.5	1.02	-3.77
	699.4	0.60	-7.67
	695.3	0.28	-9.09
	692.9	0.29	-9.80
	691.1	1.37	-5.23
	622.8	6.93	-2.39
	621.6	6.83	-2.26
	620.1	6.56	-2.78
	618.5	7.24	-1.95
	617.0	6.72	-2.64
	615.5	6.79	-2.85
	613.9	6.25	-3.09
	612.4	6.69	2.30
	611.9	6.53	-2.66
	610.4	6.73	-2.88
	608.8	6.82	-2.77
	607.7	6.78	-2.76
	605.3	6.68	-2.91
	604.2	6.93	-2.35
	602.7	6.98	-2.24
	601.2	6.62	-2.36

	599.6	6.92	-2.76
	598.1	6.50	-2.41
	596.6	5.91	-2.48
	595.4	6.26	-3.02
	593.9	5.09	-4.13
	592.0	5.47	-3.88
	589.4	6.43	-4.10
	587.9	6.44	-3.83
	584.8	6.63	-3.33
	583.3	6.41	-3.15
	581.8	6.38	-2.22
	580.2	6.32	-3.70
	578.7	6.18	-3.53
	577.2	6.31	-3.33
	576.2	6.47	-3.10
	574.6	6.30	-3.71
	573.1	5.98	-4.30
	571.6	5.94	-4.46
	570.0	5.95	-4.05
	569.5	5.75	-4.65
	499.4	4.09	-5.67
	499.0	4.68	-3.57
	498.5	5.20	-2.40
	497.7	5.01	-2.37
	497.0	4.93	-2.65

	496.4	4.79	-3.20
	495.7	4.80	-3.17
	495.1	4.60	-3.61
	493.6	4.68	-3.22
	492.3	4.47	-3.15
	491.7	4.31	-3.78
	491.0	3.83	-4.15
	490.3	3.49	-5.40
	439.5	5.55	-4.53
	426.7	6.65	-1.92
	418.4	5.63	-2.76
	414.2	6.31	-2.87
	408.5	6.07	-1.76
	405.2	5.92	-1.84
	403.3	6.47	-2.87
	400.5	6.09	-1.88
	396.3	6.45	-2.60
	393.0	6.49	-2.08
	389.7	7.38	-0.62
	382.9	7.15	-2.66
	378.4	5.74	-1.98
	372.1	7.11	-0.47
	367.9	6.29	-2.57
	362.9	6.25	-1.85
	359.0	7.21	-1.02

	356.1	6.85	-1.19
	354.0	6.38	-1.70
	351.6	7.06	-1.93
	346.5	5.64	-3.56
	345.2	6.47	-2.12
	343.6	6.63	-1.46
	336.4	6.52	-1.14
	333.1	6.61	-1.47
	330.8	5.89	-1.43
	328.3	6.58	-1.84
	326.2	6.65	-2.05
	324.5	6.42	-2.06
	322.6	6.25	-2.23
	321.4	6.38	-2.54
	320.5	6.41	-3.08
	318.9	6.38	-2.52
	314.1	6.32	-2.36
	162.2	4.17	-4.04
	160.7	3.93	-4.19
	158.2	3.92	-4.05
	157.7	4.00	-3.85
	155.8	4.12	-3.52
	153.8	3.89	-3.32
	152.0	3.83	-4.43
	150.8	3.86	-4.97

	149.3	3.20	-6.58
	139.0	2.50	-6.22
	137.5	4.41	-2.84
	136.0	4.64	-1.34
	134.6	3.50	-2.93
	133.1	3.82	-2.87
	131.6	4.02	-4.51
	130.3	3.06	-5.16
	128.9	-0.54	-5.00
	117.8	-0.33	-5.72
	116.0	-0.75	-5.36
	112.1	-1.55	-4.93
	109.8	-2.20	-5.05
	107.5	0.95	-5.95
	106.0	1.14	-6.00
	104.5	1.21	-5.28
	103.0	0.80	-5.23
	102.0	0.87	-5.71
	100.3	1.00	-5.14
	97.8	0.58	-5.97
	95.6	1.13	-5.96
	94.4	1.01	-4.77
	92.7	0.41	-6.02
	91.2	0.85	-6.01
	90.6	0.54	-6.35

	88.0	0.82	-5.14
	86.3	0.78	-5.65
	84.8	0.85	-5.31
	83.5	0.66	-6.09
	82.0	0.82	-5.76
	80.3	0.45	-5.90
	78.9	1.01	-5.37
	77.1	0.67	-4.91
	74.5	-0.48	-4.07
	72.8	-0.47	-2.90
	71.0	-0.49	-3.12
	69.2	-1.76	-4.33
	66.3	-2.94	-4.45
	64.7	-1.83	-5.31
	61.5	-1.99	-5.15
	60.2	-3.05	-4.97
	58.7	-4.03	-5.32
	56.7	-4.84	-5.08
	38.4	-4.39	-4.79
	37.1	-3.04	-4.11
	36.2	-2.44	-3.85
	34.8	-2.47	-4.04
	33.2	-0.82	-1.72
	32.4	-3.24	-8.19
	31.7	-2.81	-4.58

	29.4	-1.03	-4.63